The Metallic State in Neutral Radical Conductors: Dimensionality, Pressure and Multiple Orbital Effects

Di Tian,[†] Stephen M. Winter,[‡] Aaron Mailman,[‡] Joanne W. L. Wong,[‡] Wenjun Yong,[#] Hiroshi Yamaguchi,[§] Yating Jia,[‖] John S. Tse,[⊥] Serge Desgreniers,[▽] Richard A. Secco,[#] Stephen R. Julian,[†,○] Changqing Jin,[‖] Masaki Mito,[§] Yasuo Ohishi,[□] and Richard T. Oakley*[,‡]

[†]Department of Physics, University of Toronto, Toronto, Ontario M5S 1A7 Canada

[‡]Department of Chemistry, University of Waterloo, Waterloo, Ontario N2L 3G1, Canada

[#]Department of Earth Sciences, University of Western Ontario, London, Ontario N6A 5B7, Canada

[§]Faculty of Engineering, Kyushu Institute of Technology, Kitakyushu 804-8550, Japan

[‖]Institute of Physics, Chinese Academy of Sciences, Beijing, 100080, China

[⊥]Department of Physics, University of Saskatchewan, Saskatoon, Saskatchewan S7N 5E2, Canada

[▽]Department of Physics, University of Ottawa, Ottawa, Ontario K1N 6N5, Canada

[○]Canadian Institute for Advanced Research, Toronto, Ontario M5G 1Z8, Canada

[□]Materials Science Division, Japan Synchrotron Radiation Research Institute, SPring-8, Sayo, Hyogo 679-5198, Japan

ⓢ *Supporting Information*

ABSTRACT: Pressure-induced changes in the solid-state structures and transport properties of three oxobenzene-bridged bisdithiazolyl radicals **2** (R = H, F, Ph) over the range 0−15 GPa are described. All three materials experience compression of their π-stacked architecture, be it (i) 1D ABABAB π-stack (R = Ph), (ii) quasi-1D slipped π-stack (R = H), or (iii) 2D brick-wall π-stack (R = F). While R = H undergoes two structural phase transitions, neither of R = F,

Ph display any phase change. All three radicals order as spin-canted antiferromagnets, but spin-canted ordering is lost at pressures <1.5 GPa. At room temperature, their electrical conductivity increases rapidly with pressure, and the thermal activation energy for conduction E_{act} is eliminated at pressures ranging from ∼3 GPa for R = F to ∼12 GPa for R = Ph, heralding formation of a highly correlated (or bad) metallic state. For R = F, H the pressure-induced Mott insulator to metal conversion has been tracked by measurements of optical conductivity at ambient temperature and electrical resistivity at low temperature. For R = F compression to 6.2 GPa leads to a quasiquadratic temperature dependence of the resistivity over the range 5−300 K, consistent with formation of a 2D Fermi liquid state. DFT band structure calculations suggest that the ease of metallization of these radicals can be ascribed to their multiorbital character. Mixing and overlap of SOMO- and LUMO-based bands affords an increased kinetic energy stabilization of the metallic state relative to a single SOMO-based band system.
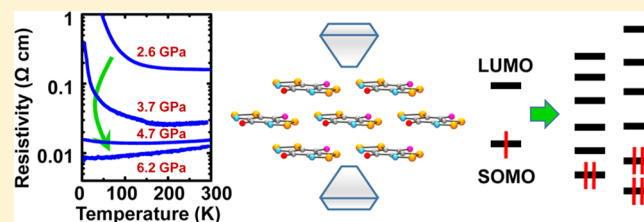
■ INTRODUCTION

The idea that organic radicals might serve as building blocks for molecular metals, with the single unpaired electron supplied by the radical acting as a carrier of charge, akin to the valence electron in an elemental metal such as sodium, has a long history.[1] Despite the apparent simplicity of the model, however, isolation of a crystalline radical with a metallic ground state has proven to be a formidable challenge.[2] Progress has been slowed by a litany of design problems, the most notable being that S = 1/2 radicals tend to associate into S = 0 dimers, through localized or delocalized (pancake) bonds,[3,4] with a consequent loss of potential charge carriers. Over the years, methods to suppress dimerization, by the judicious use of heteroatoms, spin delocalization, and steric protection have been developed. However, when dimerization is overcome, a second and more serious obstacle emerges. In a lattice composed of discrete radicals, each with one unpaired electron, there is an intrinsically large onsite Coulomb repulsion U associated with site-to-site charge migration. In addition, the pervasive weakness of intermolecular interactions between organic molecules results in a low solid-state electronic bandwidth W. Under these circumstances, that is, when the onsite repulsion exceeds some critical value U_C, such that $U > U_C \sim W$, the unpaired electrons have insufficient kinetic energy to overcome the barrier to charge transport. They are trapped on the radicals, and a Mott insulating state prevails.[5]

Over the years, the task of redressing the potential/kinetic energy (U/W) balance, in order to break out of the Mott insulating regime, has been approached in several ways. Haddon has shown that in mixed-valence spiroconjugated bisphenalenyl radicals,[6,7] the effective Coulomb potential U_{eff} is markedly reduced compared to simple phenalenyl derivatives, and the resulting materials are more conductive, with room-temperature conductivity σ_{RT} values reaching as high as ~0.3 S cm^{-1}.[8] In these systems, multiple orbitals in the vicinity of the Fermi level provide additional charge degrees of freedom that allow electrons to conduct while nearly avoiding one another in space. By contrast, the approach we have followed focuses on promoting intersite hopping, and hence W, by building radicals containing heavy (principal quantum number, PQN $\geq$ 3) p-block heteroatoms,[9] whose more diffuse valence orbitals should afford stronger intermolecular overlap between neighboring singly occupied molecular orbitals (SOMOs). Thus, for example, while early work on the resonance stabilized bisdithiazolyls **1** (Figure 1) found them to be Mott insulators,
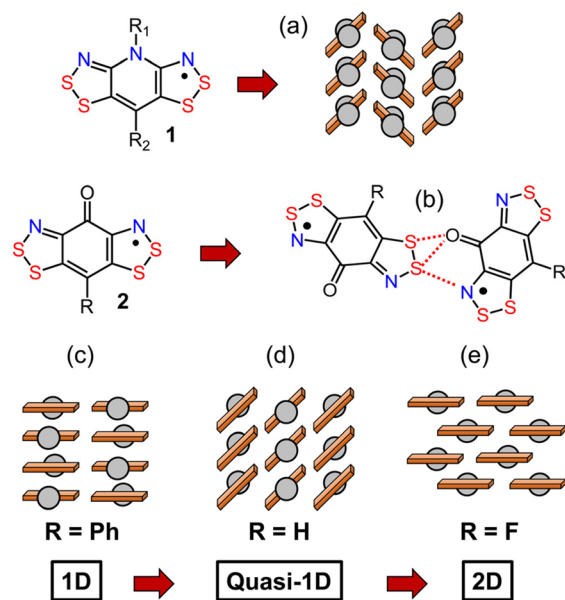
Figure 1. *N*-alkyl-pyridine- and oxobenzene-bridged bisdithiazolyl radicals **1** and **2**. (a) Herringbone packing pattern found for **1** and (b) ribbon-like arrays of **2** generated by lateral S···N′ and S···O′ supramolecular synthons. Packing patterns generated from overlaid ribbons of **2** include (c) superimposed 1D ABABAB π-stacks (R = Ph), (d) quasi-1D slipped ribbon π-stacks (R = H), and (e) 2D brick-wall π-stacks (R = F); the exocyclic oxygen atoms are colored gray.

with large charge gaps $\Delta_C = U - W$ near 0.5 eV, replacement of sulfur by its heavier congener selenium reduced the value of Δ_C substantially.[10,11] Moreover, for some Se-based systems the residual charge gap could be completely closed in compacted powder samples by applying physical pressure (~10 GPa).[12] In the resulting "bad metal" states, the thermal activation energy for conduction was reduced essentially to zero, but the conductivity itself remained much lower than that expected for a Fermi liquid metal, perhaps due to the granular nature of samples and/or the one-dimensional (1D) character of the electronic structure. In the absence of pressure, and at low temperatures, these heavy atom radicals can display strong magnetic exchange interactions, which give rise to magnetically ordered phases with relatively high ordering temperatures.[13,14]

More recently, and with the intent of increasing bandwidth (kinetic energy stabilization), we explored variants of **1** in which the bridging *N*-pyridyl moiety is replaced by an oxobenzene unit, as in **2**. The original purpose of this modification was to disrupt the herringbone packing patterns (Figure 1a) typical for **1**, which result in relatively 1D electronic structures, and thus small U_C/W ratios. This was accomplished by using lateral S···N′ and S···O′ supramolecular synthons[15] to generate coplanar zigzag chains of radicals (Figure 1b). Consistently, the crystal structures of **2** (R = H, F, Cl, Br, I, Me, Ph)[16,17] are all characterized by ribbon-like arrays of radicals overlaid to afford, inter alia, (i) 1D ABABAB π-stacks (R = Ph), quasi-1D slipped ribbon π-stacks (R = H), or perfectly 2D brick-wall π-stacks (R = F). Regardless of the packing pattern observed, the charge-transport properties of these materials are uniformly better, with values of σ_{RT} at ambient pressure ranging from 10^{-4} to 10^{-2} S cm^{-1}, compared with ~10^{-6} S cm^{-1} for most derivatives of **1**. Moreover, while the conductivity remains activated, the charge gap Δ_C, estimated from thermal activation energies E_{act}, falls to between 0.2 and 0.1 eV.

Initially, we interpreted the improved performance of **2** relative to **1** in terms of an increase in bandwidth and dimensionality of the solid-state electronic structure occasioned by the change in packing. In so doing, however, we assumed that the electronic properties of the two building blocks were essentially the same, a position supported by the near equality of U-values calculated by density functional theory (DFT) methods.[18] However, inspection of the electrochemical behavior of **1** and **2** suggested otherwise. For example, the experimental cell potential E_{cell} of 0.56 V for **2** (R = H) compared to 0.77 V for **1** (R$_1$ = Me, R$_2$ = H) pointed to a substantially lower Coulomb barrier for **2**.[16e] Subsequent exploration of the discrepancy between the computational and electrochemical estimates of U revealed a fundamental difference between the molecular electronic structures of **1** and **2** occasioned by the replacement of the NR moiety by a CO group; it is not a simple isolobal[19] exchange. While incorporation of the carbonyl group does not perturb the SOMO, as witnessed by the similarity in the EPR hyperfine coupling constants in the two radicals, mixing of the CO π*-orbital results in a low-lying empty π-LUMO,[20] the presence of which has a major impact on both the magnetic,[21] and charge-transport properties of derivatives of **2**.[20] This second orbital influences charge-transport properties in two ways. First, the additional orbital degrees of freedom provide flexibility for the electrons to avoid one another, thus reducing the effective Coulomb repulsion, and second, hopping to and from this extra orbital provides additional pathways for conduction, enhancing the effective kinetic incentive for delocalization.

With these issues in mind we have carried out a study of the pressure dependence of the transport properties of the set of radicals **2** (R = H, F, Ph), whose packing motifs span the spectrum of electronic dimensionality from 1D to 2D (Figure 1c−e). The observation of metallic conductivity in the $T \rightarrow 0$ K limit is the gold standard for demonstrating that metallization has been achieved, and pressure is a particularly effective tool for investigating metal−insulator transitions.[22] In the present case, the use of pressure allows us to study crystalline molecular radicals with low levels of disorder that can mask the intrinsic metal−insulator transition due to localization by scattering or contributing conducting states in the gap. Pressure-induced transitions to bad metal states are observed for all three radicals,

with the critical pressure decreasing with increasing dimensionality from near 12 GPa (R = Ph) to 3 GPa (R = F). In the case of R = F at 6.2 GPa, a wide region (T = 5−300 K) of quasiquadratic temperature dependence of the resistivity has been identified, which may be interpreted in terms of 2D Fermi liquid state. DFT band structure calculations on all three radicals at different pressures have been used to identify the factors that lead to kinetic energy stabilization of the metallic state.

■ RESULTS AND DISCUSSION

Theoretical Model. Before presenting the results of structural and transport property measurements under pressure, we first describe the basic electronic differences between multiorbital radicals such as **2** and conventional single orbital radicals typified by **1**. As indicated above, the presence of the low-lying LUMO in **2** affects charge transport in two ways, by (i) reducing the potential barrier to charge migration and (ii) enhancing the effective kinetic incentive for charge delocalization. The first of these roles can be understood by considering the ionic states associated with site-to-site electron transfer in a system based on two orbitals per site (Figure 2), in which the SOMO and LUMO on each site are separated by an energy difference $\Delta\varepsilon$, and electrons in different orbitals feel a reduced repulsion $V < U$.
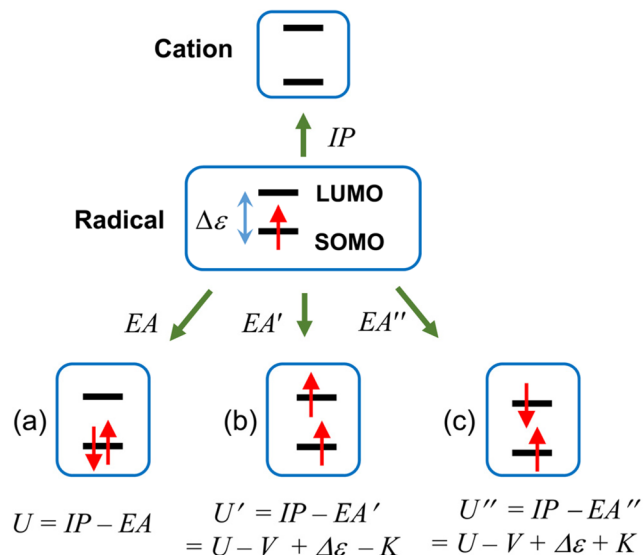
Figure 2. Ionic states and energetic changes associated with site-to-site charge transfer involving a radical with two orbitals per site. Only one cationic state may be formed, but three anionic states (a) closed-shell, (b) triplet, and (c) open-shell singlet are possible. The resulting values of U, U', and U'' are defined in terms of the SOMO−LUMO energy separation $\Delta\varepsilon$, electron repulsion V between electrons in different orbitals, and the electron exchange term K.

Oxidation of either radical **1** or **2** affords a single closed-shell cationic state with an ionization potential IP, regardless of whether a second orbital (LUMO) is present.[23] In the absence of a low-lying LUMO on the radical, as in **1**, only the closed-shell singlet option is available for the anion, and the resulting value of EA and hence $U = IP − EA$ is uniquely specified. However, with the introduction of a low-lying virtual orbital, as in **2**, reduction can lead to three possible anions, a closed-shell singlet, a triplet, and open shell singlet, each of which is

associated with a different electron affinity. The respective electron affinities EA' and EA'' of these additional states and the resulting values of U' and U'' are then dependent on the repulsion V between electrons in different orbitals and the magnitude of the electron exchange term K, that is, Hund's rule coupling.[24] Broken symmetry BS-DFT calculations on **2** (R = H) suggest a triplet ground state,[20] with the corresponding value of U' being ∼0.2 eV lower than U, in accord with the lower E_{cell} value observed electrochemically.[16e] In contrast, gas-phase CI calculations on **2** (R = F) suggest a singlet ground state for the molecular anion, but nonetheless provide estimates of $U − V \sim 0.24$ eV, $\Delta\varepsilon \sim 0.6$ eV, and $K \sim 0.2$ eV consistent with a very low-lying triplet state.[21]
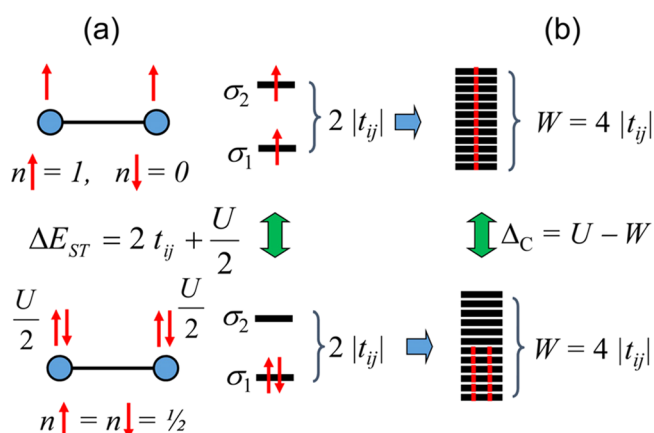
Figure 3. (a) Two-site two-orbital Hubbard model applied to a pair of radicals, with singlet−triplet splitting ΔE_{ST} expressed in terms of the onsite Coulomb repulsion U and interorbital hopping (resonance) integral t_{ij}; $n_\uparrow$ and $n_\downarrow$ represent the fraction of spin $\uparrow$ and spin $\downarrow$ on each radical, and $\sigma_{1,2}$ are the bonding and antibonding combinations of radical SOMOs. (b) Charge gap Δ_C between the Mott insulating and metallic states associated with an infinite 1D array of radicals, assuming a uniform distribution of orbital energies.

While the existence of such low-lying open-shell states has important consequences on the magnetic behavior of these radicals,[17] their role, in the context of charge transport, is to provide additional channels for conduction, with potentially lower effective Coulomb barriers $U_{eff} = U'$ and U'', thus facilitating the Mott insulator to metal (MI) transition. From the perspective of the metallic side of this transition, these additional channels are manifest in the overlap and hybridization of the energy bands derived from the SOMO and LUMO in the solid state,[21] which enhances the kinetic incentive for delocalization. To explore the magnitude of this effect, we begin by reviewing the origin of kinetic stabilization of the metallic state in a simpler system, specifically a 1D chain of one-orbital radicals, as in a π-stacked array of **1**. With reference to the two-site Hubbard model (Figure 3),[25] the energy difference between the closed-shell singlet and triplet states ΔE_{ST} of a pair of neighboring radicals may be expressed in terms the Coulomb repulsion associated with charge localization onto the same site ($U/4$ per site) and kinetic stabilization (bonding energy) occasioned by intersite hopping (t_{ij} per site), where t_{ij} is the hopping or resonance integral. The degeneracy point occurs when $U = 4 |t_{ij}|$, with larger values of U favoring breaking of the bond, to form a pair of radicals, a process analogous to the metal to Mott insulator transition in the solid state.

One may extrapolate this condition to an infinite array of radicals if one assumes a solid-state band of width $W = 4 |t_{ij}|$ with a constant density of states $D(\varepsilon) = (d\varepsilon_k/dk)^{-1}$. In this case, the per-site mean-field energies of the Mott insulating and metallic states are simply $E_{ins}/N = \varepsilon_0$ and $E_{met}/N = \varepsilon_{ave} + U/4$, where ε_{ave} is the average kinetic energy of electrons in the metallic state as defined in eq 1, N is the number of sites, $\varepsilon_F = \varepsilon_0$ is the orbital energy of the SOMO, and $\varepsilon_B = 2 t_{ij}$ is the energy of the lowest occupied orbital in the band. For a constant density of states, $E_{met} = \varepsilon_0 - |t_{ij}| + U/4$, and the critical Coulomb repulsion U_C at the Mott transition should correspond closely with the degeneracy point $E_{ins} = E_{met}$, suggesting a value of $U_C \sim W$.

$$\varepsilon_{ave} = \frac{1}{N} \int_{\varepsilon_B}^{\varepsilon_F} \varepsilon \cdot D(\varepsilon) d\varepsilon \tag{1}$$

For a generic density of states, the above prescription of $W = 4|t_{ij}| > U$ for the onset of the metallic state can be improved by explicit calculation of ε_{ave} via eq 1. For example, in a simple 1D system where $\varepsilon_k = \varepsilon_0 - 2t_{ij} \cos(ka)$, $D(\varepsilon)$ is a minimum at the Fermi level ε_F and increases asymptotically toward the edges of the band (Figure 4). As a result the overall kinetic energy stabilization (per site) is enhanced, with $\varepsilon_{ave} = (4/\pi) t_{ij}$,[26] suggesting $U_C \sim (4/\pi)W \sim 1.3 W$. By contrast, in a single orbital 2D square lattice with nearest-neighbor hopping integral t_{ij}, $D(\varepsilon)$ is a maximum at the Fermi level, and the bandwidth $W = 8|t_{ij}|$. For this case, the simple analysis above gives $U_C \sim 0.8W = 0.64|t_{ij}|$, slightly smaller than W, but in agreement with the results of more sophisticated numerical methods.[27] Finally, it is worth noting that the discussion so far has neglected the first-order nature of the Mott transition,[28] which implies a finite range of U/W where both the insulating and metallic states are stable at low temperature. Moreover, we have not considered the role of short-range charge fluctuations, which stabilize the Mott insulator, and result in magnetic exchange interactions between localized spins. Indeed, if such effects are included one might expect the energy of the insulator to go as $E_{ins}/N \sim \varepsilon_0 - O(t_{ij}^2/U)$, which implies an extended magnetically ordered phase, and reduction in U_C by as much as a factor of 2.
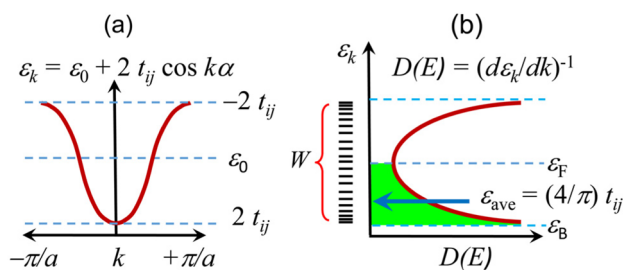
Figure 4. (a) Orbital energy dispersion function and half-filled energy band for a 1D array of radicals, evenly spaced at a distance a, with SOMO energy ε_0 and hopping integral t_{ij}. (b) The resulting $D(\varepsilon)$ function has an average occupied orbital energy $\varepsilon_{ave} = (4/\pi) t_{ij}$. The energies of the highest and lowest occupied levels are $\varepsilon_F = \varepsilon_0$ and $\varepsilon_B = 2 t_{ij}$, respectively.

Despite variations in U_C for the above single-orbital examples, the use of the $W > U$ criterion for metallization represents a reasonable working axiom; wider bands increase kinetic stabilization of the metallic state, reduce the charge gap, and increase conductivity. However, in multiorbital radicals like **2**, hybridization of the low-lying virtual orbital with the SOMO

provides additional kinetic stabilization of the metallic state, as long as the energy difference between the two orbitals ($\Delta\varepsilon$) is comparable to the hopping integrals between adjacent SOMOs (t_{ij}^{00}), LUMOs (t_{ij}^{11}), and SOMO–LUMO pairs (t_{ij}^{01}/t_{ij}^{10}). To see this, note that the mean-field energy of the insulator $E_{ins} = \varepsilon_0$ is precisely the same as in the single orbital case; electrons are localized into the SOMO at each site, and all hopping is blocked by Coulomb repulsion, so that the LUMO remains essentially unoccupied. In the metallic state, however, interorbital hopping generally results in the mixing of the two orbitals to form several partially occupied hybrid bands intersecting the Fermi level. Thus, in contrast to the one-orbital model, where the Fermi level ε_F in the metallic state can be equated with ε_0, the Fermi level in the two-orbital model is lowered (stabilized) as electrons are redistributed between the SOMO and LUMO (Figure 5). In terms of the resulting shift in the chemical potential $\Delta\mu = \varepsilon_0 - \varepsilon_F$ and the dispersion energy $\varepsilon_{dis} = \varepsilon_F - \varepsilon_{ave}$, the energy of the metallic state may be estimated by $E_{met} = \varepsilon_0 - (\varepsilon_{dis} + \Delta\mu) + U_{eff}/4$, where $U_{eff} < U$ due to partial occupation of both bands, as discussed above. Thus, the critical value of the Coulomb repulsion, corresponding to $E_{ins} = E_{met}$, is generally much greater than the single orbital case and specifically must exceed $U_C > 4 \varepsilon_{dis} + 4 \Delta\mu$. In this latter expression, the first term is analogous to the single-orbital bandwidth W, while the chemical potential shift $\Delta\mu$ is a purely "multiorbital" effect. The role of these various terms in determining the electronic structure of **2** as a function of pressure is developed below, following the presentation of transport property and structural measurements.
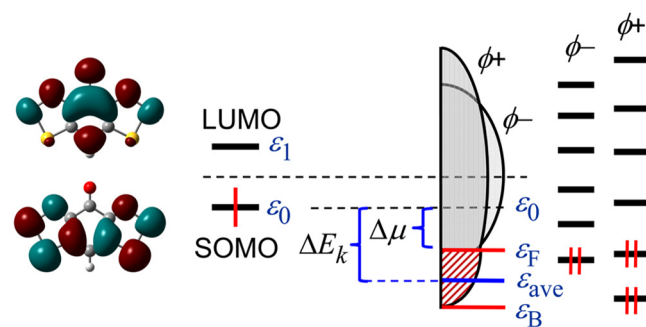
Figure 5. Cartoon of the overlap of energy bands arising from combinations ϕ^+, ϕ^- of the Kohn–Sham SOMO and LUMO of the multiorbital radical **2** (R = H) and the kinetic stabilization ($\Delta E_k = \varepsilon_0 - \varepsilon_{ave}$) of the metallic state afforded by (i) band dispersion $\varepsilon_{dis} = \varepsilon_F - \varepsilon_{ave}$, and (ii) electron redistribution $\Delta\mu = \varepsilon_F - \varepsilon_0$ between the two bands.

Powder Crystallography. The crystal structures of **2** (R = H, F, Ph) at ambient pressure (0 GPa) were determined previously by single crystal X-ray diffraction methods.[16a,d,e] All three structures belong to polar orthorhombic space groups: $Fdd2$ for R = H, $Cmc2_1$ for R = F, and $P2_12_12_1$ for R = Ph. Figure 6 shows unit cell drawings and illustrates the ribbon-like arrays of radicals laced together by intermolecular S···N′ and S···O′ interactions of the type shown in Figure 1b. These ribbons are then overlaid to form either slipped π-stack arrays (R = H), 1D superimposed ABABAB π-stacks (R = Ph), or brick-wall π-stack motifs (R = F), as illustrated in Figure 1c–e.

In previous work the effect of pressure on the structure of **2** (R = H) was examined over the range 0–13 GPa by powder X-ray diffraction, using synchrotron radiation and diamond anvil
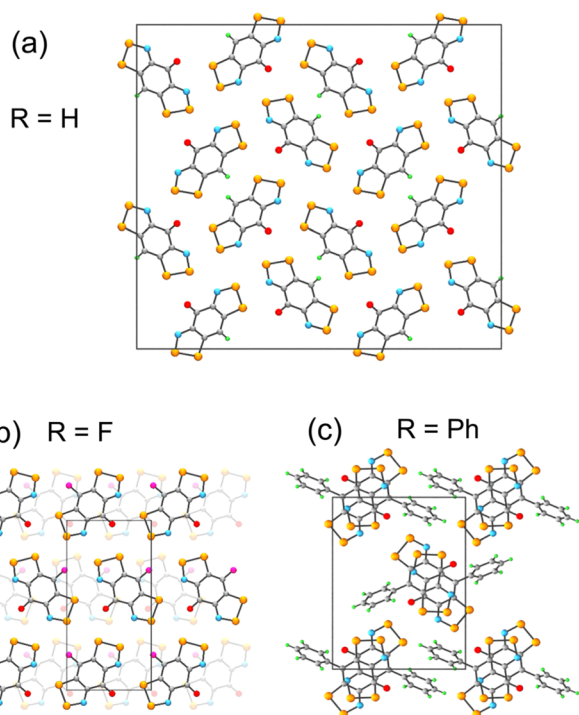
Figure 6. Unit cell drawings of **2** with (a) R = H, (b) R = F, and (c) R = Ph at ambient pressure, showing ribbon-like arrays of radicals.

cell (DAC) techniques. In addition to the ambient pressure or α-phase (space group *Fdd2*), which is stable up to 3−4 GPa, two new phases were identified.[20] Above 4 GPa a second or β-phase is formed, in which *F*-centering is lost and the space group symmetry lowered to *Pbn2₁*, with a concomitant halving of the *a* and *b* axes (Figure 7). The changes in packing that accompany this phase transition may be viewed in terms of an "ironing out" of the ruffled ribbon-like architecture of the α-
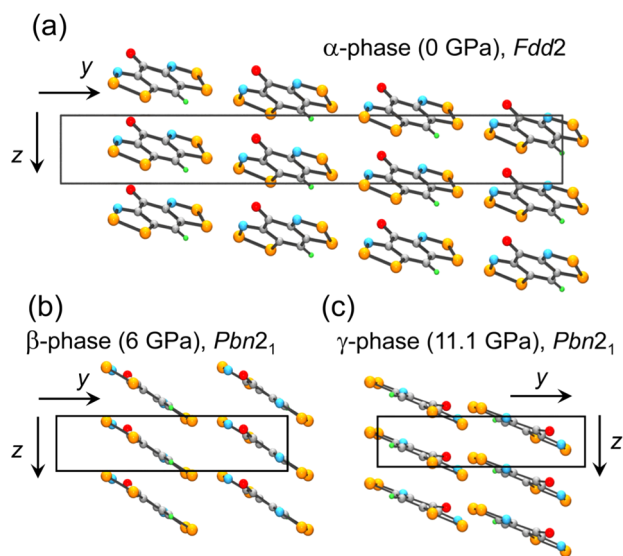
Figure 7. Pressure-induced phases of **2** (R = H). (a) Side view (along *x*) of 1D π-stacks in the α-phase (space group *Fdd2*), with ruffled ribbons of radicals propagated by the *d*-glides. (b) In the β-phase (space group *Pbn2₁*), the coplanar ribbons are related by *b*-glides (and translation along *z*). (c) In the γ-phase (space group *Pbn2₁*) the ribbons follow the *n*-glides.

phase, so that consecutive radicals along the ribbons are rendered more nearly coplanar. In the β-phase the planar ribbons are propagated along the *b*-glides. In the third or γ-phase, also space group *Pbn2₁*, generated by compression beyond to 8 GPa, the quasi-planar ribbons follow the *n*-glides.

High-pressure (HP) crystallographic studies have now been performed on **2** (F, Ph), again using synchrotron radiation and DAC techniques. Powder diffraction data were collected at room temperature as a function of *increasing* pressure up to 10 GPa, with helium as the pressure transmitting medium. As may be seen in Figure 8, which provides "waterfall" plots of the
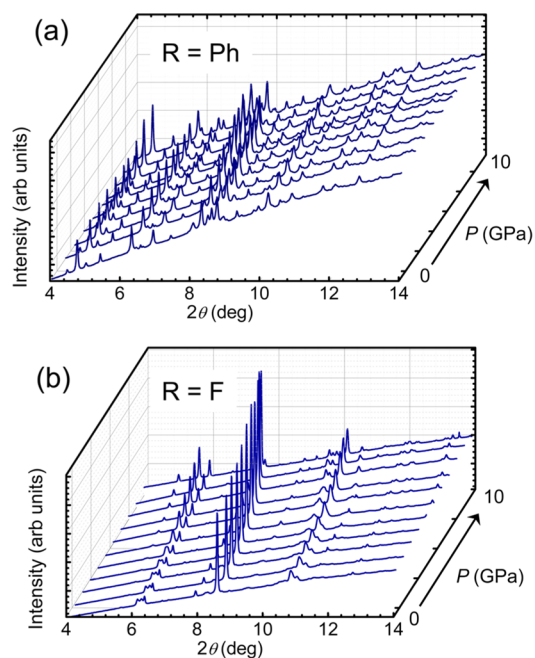

Figure 8. X-ray powder diffraction patterns (λ = 0.41244 Å) for (a) **2** (R = Ph) and (b) **2** (R = F), recorded at regular pressure intervals from 0 to 10 GPa.

diffraction patterns for the two compounds, the retention of resolution and the smooth and steady evolution of the positions of the diffraction peaks with increasing pressure indicates that no phase change has occurred as a result of compression and that there has been no degradation of the samples. The data sets so obtained were indexed, and the structures solved in DASH using molecular models derived from the ambient pressure single crystal solutions. During the initial Rietveld refinements (in DASH) a rigid-body constraint was employed, but in the final Rietveld refinements (in GSAS) only the unit cell parameters were optimized. A sampling of the crystal data from the final powder refinements at selected pressures is summarized in Table 1 (a full listing is provided in Table S1). Variations in the unit cell dimensions of **2** (R = Ph, F) as a function of pressure are shown in Figure 9. All three axes contract, the most significant response being parallel to the *a*-axis, as found previously for R = H, an observation which reflects the relative ease of compression of the layered π-stacks. Not surprisingly the 2D brick-wall architecture of the R = F derivative is somewhat more rigid (less compressible) than either R = Ph or H. In the more 1D structure of R = Ph there is no indication of dimerization along the ABABAB π-stacks, as has been observed in derivatives of **1** with alternating π-stack architectures.[29] Pressure-induced changes in the lateral

Table 1. Crystal Data

	2 (R = F)[a]	2 (R = F)	2 (R = F)	2 (R = F)	2 (R = Ph)[b]	2 (R = Ph)	2 (R = Ph)
formula	$C_6FN_2OS_4$	$C_6FN_2OS_4$	$C_6FN_2OS_4$	$C_6FN_2OS_4$	$C_{12}H_5N_2OS_4$	$C_{12}H_5N_2OS_4$	$C_{12}H_5N_2OS_4$
fw	263.32	263.32	263.32	263.32	321.42	321.42	321.42
press, GPa	0	2.0	4.3	6.1	0	5.2	10.2
a, Å	6.3010(13)	6.02602(7)	5.79339(7)	5.6811(15)	6.8011(7)	5.98941(15)	5.71784(18)
b, Å	7.9210(16)	7.7738(4)	7.6413(6)	7.5876(21)	11.3785(12)	10.8833(4)	10.6889(6)
c, Å	15.916(3)	15.5993(19)	15.345(4)	15.249(9)	15.6252(16)	14.8019(11)	14.4886(14)
V, Å³	794.4(3)	730.74(7)	679.29(16)	657.3(6)	1209.2(2)	964.85(6)	885.50(7)
space group	$Cmc2_1$	$Cmc2_1$	$Cmc2_1$	$Cmc2_1$	$P2_12_12_1$	$P2_12_12_1$	$P2_12_12_1$
Z	4	4	4	4	4	4	4
temp, K	293(2)	296(2)	296(2)	293(2)	296(2)	296(2)	296(2)
λ, Å	0.68890	0.41244	0.41244	0.41244	0.71073	0.41244	0.41244
solution method	direct methods	powder data	powder data	powder data	direct methods	powder data	powder data
R_p	0.0534	0.0038	0.0044	0.0049	0.0547	0.0027	0.0029
R_{wp}	0.1253	0.0052	0.0063	0.0075	0.0739	0.0040	0.0041

[a]Single crystal data, ref 16d. [b]Single crystal data, ref 16a.
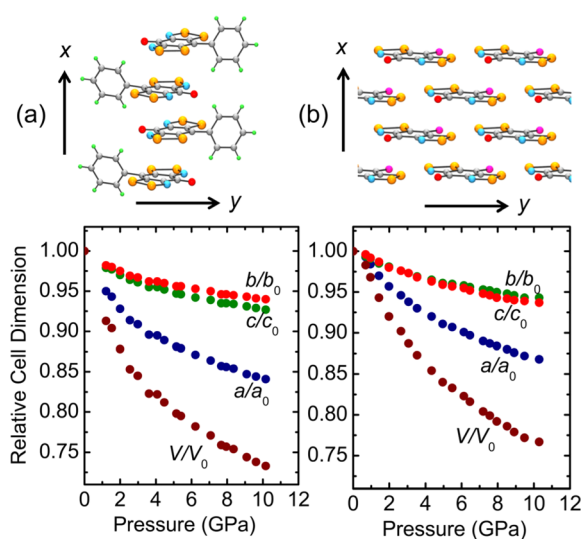
Figure 9. Contraction in unit cell dimensions of (a) 2 (R = Ph) and (b) 2 (R = F) over the pressure range 0−10 GPa. In both cases compression is preferred parallel to the a-axis, which corresponds to the π-stacking direction.

intermolecular S···N′, S···O′, and S···F′ contacts are provided in Figures S12 and S13. For all three compounds, the collective changes in electronic structure induced by pressure are discussed below.

Magnetic Measurements. At ambient pressure, all three radicals 2 (R = H, F, Ph) order as spin-canted antiferromagnets (SC-AFMs), with ordering temperatures T_N of 4 K (R = H), 13 K (R = F), and 4.5 K (R = Ph).[16a,d,e] In the case of R = F the simplicity and high symmetry of the crystal structure permit an absolute identification of the magnetic cell.[21] In such organic materials, where isotropic magnetic interactions dominate, spin canting may only occur without additional symmetry breaking, implying that any two sites related by translation must belong to the same magnetic sublattice. For 2 (R = F), this condition implies strong ferromagnetic (FM) interactions within the 2D layers of π-stacked radicals related by C-centering, the origin of which was rationalized[21] in terms of multiorbital contributions[30] to the magnetic exchange. As shown elsewhere,[17] the nearest-neighbor magnetic exchange for the multiorbital radical may be described by $H = -2J_{ij}S_i \cdot S_j$, where the exchange constant J_{ij} is defined in eq 2.

$$2J_{ij} = -4\frac{(t_{ij}^{00})^2}{U} + 2\frac{(t_{ij}^{10})^2 + (t_{ij}^{01})^2}{(V + \Delta\varepsilon)^2 - K^2} \tag{2}$$

Accordingly, strong ferromagnetic (+ve) exchange benefits from a small SOMO−LUMO energy difference ($\Delta\varepsilon$) and a small ratio of the SOMO−SOMO hopping integral (t_{ij}^{00}) to the interorbital (SOMO−LUMO) hopping integrals (t_{ij}^{01} and t_{ij}^{10}), suggesting the potential for strong SOMO−LUMO mixing under pressure. However, with increasing pressure, both the magnetic susceptibility and ordering temperature were found to be rapidly suppressed in 2 (R = F), either due to an enhancement of competing antiferromagnetic (AFM) terms or a strong reduction of the ordered moment via frustration and/or charge fluctuation effects associated with the proximal metallic phase. To explore the generality of this finding we have now examined the effect of pressure on the SC-AFM states of 2 (R = H, Ph), using zero-field-cooled (ZFC) magnetization measurements M (at field H = 100 Oe) in a piston cylinder cell (PCC) over the range 0.0−1.5 GPa. The results, presented in Figure 10 in the form of plots of M (ZFC) against temperature at different pressures, suggest somewhat different behavior for the two materials.

The response of R = Ph is qualitatively similar to that obtained earlier for R = F.[21] The magnetization diminishes with
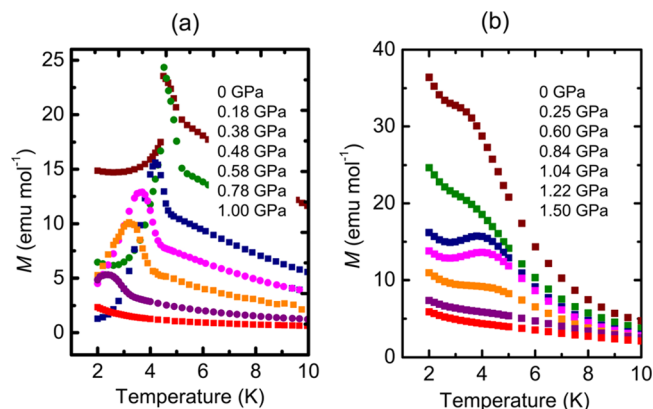
Figure 10. Plots of ZFC M versus T (at 100 Oe) as a function of pressure for 2, with (a) R = Ph and (b) R = H. In each graph pressure increases from the top to the bottom plot, with individual values shown in the legend.

increasing pressure, and the ordering temperature T_N also retreats, with the result that the spin-canted state is essentially quenched at 1 GPa. In this material, symmetry considerations place no restriction on the ambient pressure magnetic cell, although analysis of the intermolecular hopping integrals and the ambient pressure magnetic response strongly suggests FM interactions within the 1D ABABAB radical π-stacks running along the x-direction and much weaker lateral AFM interstack interactions. In this material, the large ambient pressure charge gap and unfrustrated magnetic topology suggest that suppression of M and T_N likely result from a decreasing magnitude of the FM exchange within the 1D π-stacks under pressure. For **2** (R = H), the value of M also diminishes under pressure, but there is little apparent variation in value of T_N up to 1.5 GPa, the limit of the experiment. In this material, canting may only arise if all molecules related by F-centering or within a given π-stack (running along the z-direction), belong to the same magnetic sublattice, again implying FM π-stack interactions. While the reduction of M may result from a suppression of such FM interactions under pressure, the complex structure of **2** (R = H) gives rise to a large number of likely frustrated interstack interactions,[31] implying that the gradual disappearance of the canted moment may instead be a frustration effect.
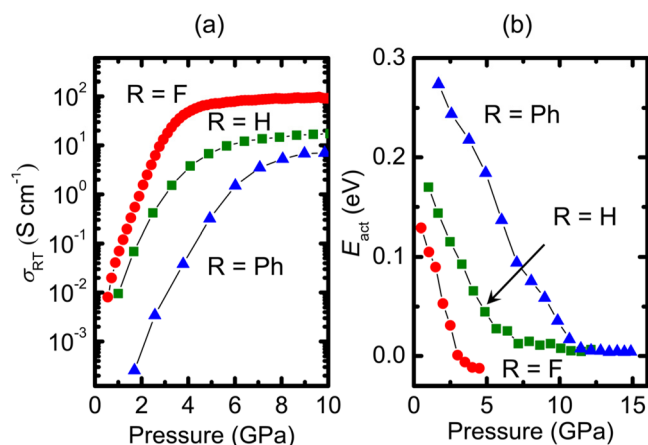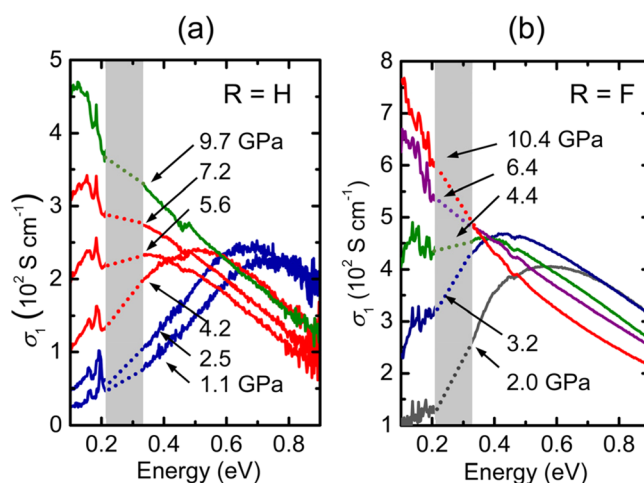

Figure 11. Pressure dependence of (a) the room-temperature conductivity σ_{RT} of **2** (R = H, F and Ph) and of (b) the thermal activation energy E_{act} over the range T = 298–370 K.

Ambient Temperature Conductivity Measurements. Initial high-pressure conductivity studies on **2** (R = H, F), performed using cubic anvil press (CAP) and multi-anvil press (MAP) techniques,[16d,20] established that the thermal activation energy for conduction E_{act}, measured over the temperature range 298–370 K, was essentially eliminated at pressures above ~3 GPa (R = F) and ~6 GPa (R = H). These results provided evidence for closure of the charge gap Δ_C and formation of a bad metal state. We have now extended these measurements to include R = Ph and have also explored the pressure dependence of the conductivity of R = F out to 10 GPa. The combined results of these CAP/MAP measurements, presented in Figure 11 in the form of plots of σ_{RT} versus P and E_{act} versus P (from data taken over the range T = 298–370 K), illustrate the pressure-induced transition from the Mott insulating state to the bad metal state, not only for R = F (near 3 GPa) and R = H (near 6 GPa) but also for R = Ph, which occurs near 12 GPa. In all three cases, the onset of the plateau region in σ_{RT}

corresponds approximately to the pressure where E_{act} is eliminated and the charge gap Δ_C vanishes. At the same time the limiting (plateau) value of the conductivity steadily increases along the series R = Ph, H, F, reaching a value near 10^2 S cm^{-1} for R = F, not far below the Mott–Ioffe Regel limit of 10^3 S cm^{-1}.[32] We attribute the steady improvement of both the closure of the charge gap and ultimate value of σ_{RT} to the increase in structural and electronic dimensionality across this series R = Ph < H < F. These issues are explored in more detail below.

Figure 12. Pressure dependence of the room-temperature optical conductivity σ_1 of **2**, (a) R = H and (b) R = F. For R = H the three phases are color coded blue (α), red (β), and green (γ). The hatched zone in both plots is obscured by diamond modes.

Ambient Temperature Optical Conductivity. To probe more closely these pressure-induced changes in electronic structure, we have examined the optical conductivity σ_1 of **2** (R = H, F) over the pressure range 0–10 GPa, using reflectivity measurements obtained on pressed powder samples in a DAC. Despite the occurrence of two structural phase transitions for R = H in this pressure range, the changes in σ_1 with pressure for the two compounds (Figure 12a,b) are qualitatively similar. At low pressures, that is, <3GPa for R = H (the α-phase) and <2 GPa for R = F, the optical conductivity reveals a broad electronic excitation band, with spectral density falling away at low frequencies, characteristic of Mott insulating behavior.[33] Accordingly the broad peak in σ_1 is centered at the energy scale for both inter- and intraorbital short-range charge fluctuations ($U_{eff} \sim 0.6$–0.8 eV) and with a spread that reflects the combined bandwidth of the empty LUMO and upper Hubbard band ($\sim 2W$). With further compression of R = H to ~4 GPa, which affords the β-phase, and of R = F to ~3 GPa, there is a large transfer of spectral weight (a shift in σ_1) to lower energies, suggesting rapid closure of the Mott gap and formation of a correlated (bad) metallic state. Finally, near 10 GPa for R = H (nominally the γ-phase) and above 6 GPa for R = F, the high-frequency Hubbard features are nearly absent, and the response appears essentially Drude-like, although σ_1 appears to decay at high frequencies more slowly than ω^{-2}.
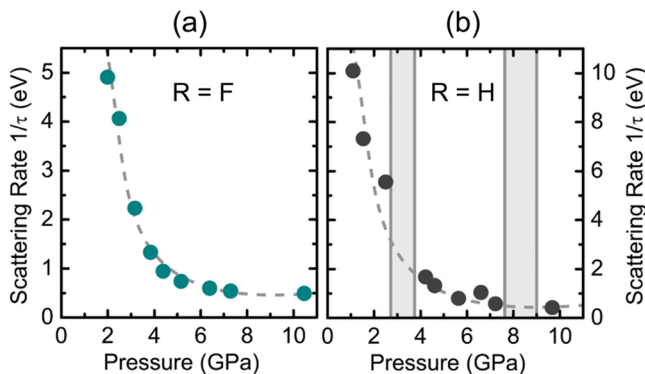
The results were further analyzed using REFFIT[34] in an extended Drude formalism[35] in order to extrapolate the effective quasiparticle scattering rate $1/\tau$ to zero frequency, as in eq 3:

$$\frac{1}{\tau} \equiv \lim_{\omega \to 0} -\frac{\omega_p^2}{\omega} \text{Im}\left[\frac{1}{\varepsilon(\omega) - \varepsilon(\infty)}\right] \qquad (3)$$

where the plasma frequency ω_p was obtained by integration of the optical conductivity, as in eq 4, and $\varepsilon(\omega)$ refers to the frequency-dependent dielectric function.

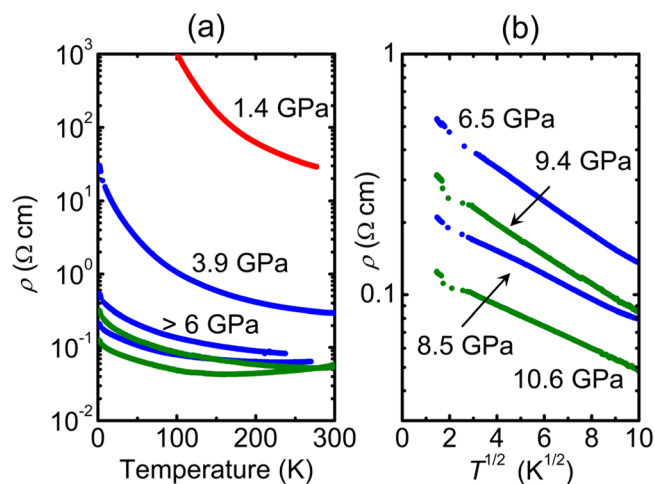$$\frac{\omega_p^2}{8} = \int_0^\infty \sigma_1(\omega)d\omega \qquad (4)$$

Despite the absence of low-frequency experimental data, this analysis of the obtained optical conductivity suggests that the scattering rate $1/\tau$ decreases by an order of magnitude for both **2** (R = F, H) over the pressure range 2−10 GPa (Figure 13), saturating above 5 GPa (R = F) and 7 GPa (R = H), consistent with the pressure dependence of the DC conductivity ($\sigma_{DC} \propto \tau$). However, even at the highest pressures, the extracted scattering rates of $\hbar/\tau \sim 0.5$ eV remain on the scale of the electronic kinetic energy, as estimated, for example, by the DFT-calculated Fermi energy (see below), implying a correlated metallic state at room temperature.

Figure 14. (a) Plots of resistivity ρ versus temperature for **2** (R = H) at different pressures, measured with a DAC. Structural phases are color-coded: red, α-phase; blue, β-phase; and green, λ-phase. (b) Log plot of ρ vs $T^{1/2}$ in the high-pressure region, showing the $\exp[-(T/T_0)^{1/2}]$ dependence of ρ below T = 100 K.

Figure 13. Pressure dependence of the scattering rate $1/\tau$ for **2**, R = F and H. The hatched regions correspond to the $\alpha \to \beta$ and $\beta \to \gamma$ phase transitions.

Overall, however, the ambient temperature optical conductivity results complement the DC measurements. That is, the shift in the spectral weight of σ_1 and the suppression of $1/\tau$ with increasing pressure provide strong evidence for a Mott insulator to metal transition in **2** (R = H, F). Future studies of the temperature dependence of σ_1 for these and related materials, as well extensions to lower frequency, may provide more information into the evolution of their electronic structure under pressure.

Low-Temperature Conductivity Measurements. As noted above, more detailed insight into the electronic structure of these radicals at elevated pressure requires exploration of their transport properties at low temperature. To this end, preliminary low-temperature conductivity measurements on R = F, performed using a piston cylinder cell (PCC), confirmed the absence of an electronic transition (to a metallic state) up to 2 GPa.[21] Access to higher pressures, however, requires the use of DAC techniques, and here we report the results of such measurements (from 5 to 300 K) on **2** (R = H, F), the two most pressure-responsive radicals under consideration. Figure 14 summarizes resistivity ρ versus T data for R = H at selected pressures up to 10 GPa. As in the optical conductivity measurements, the plots are color-coded to denote the appropriate phase (α, β, and λ), as determined crystallo-

graphically. In this light the marked reduction in the low-temperature value of ρ between 1.4 and 3.9 GPa can be related to the $\alpha \to \beta$ phase transition, while the second drop, between 3.9 and 6.5 GPa, heralds the onset of metallization of the β-phase. Between 6.5 and 8.5 GPa, ρ decreases marginally, as expected, but with continued compression to 9.4 GPa, and with the onset of the second ($\beta \to \lambda$) phase transition, there is a significant increase in resistance. This behavior is likely not electronic in origin, but rather a reflection of phase inhomogeneity in the compacted pellet in the DAC. With subsequent compression to 10.6 GPa ρ continues to drop, reaching a minimum value (at 150 K) near 0.05 Ω cm. At this pressure, the resistivity displays metallic behavior ($d\rho/dT > 0$) above 150 K, but shows an unconventional response below this temperature, with $\rho = \rho_0 \exp[-(T/T_0)^{1/2}]$ over two decades of temperature. For small (T/T_0), this form can be written $\rho \sim \rho_0[1 - (T/T_0)^{1/2}]$, which is reminiscent of the response observed in other highly disordered metals,[36] implying that the weak localization found at low temperatures in **2** (R = H) likely results from the disordered nature of the pressurized samples.

While the response of the resistivity of **2** (R = H) to pressure is complicated by structural phase transitions, there is no such problem for the corresponding R = F derivative, which maintains the same ($Cmc2_1$) phase over the entire pressure range 0−10 GPa. As a result its low temperature resistivity displays a more uniform response to pressure, and the low-temperature localization tail may be avoided at the highest pressures. The DAC measurements on this material (Figure 15a) reveal changes in ρ that are consistent with the slow evolution of the bad metal state produced near 3 GPa to a Fermi liquid state near 6 GPa. Thus, the low-temperature tail observed at 3.7 GPa is all but lost by 4.7 GPa, and at 6.2 the $\rho(T)$ profile displays a positive power law temperature dependence over the entire (5−300 K) temperature range. A purely quadratic T^2 dependence of the resistivity observed in organic[37] and inorganic[38] materials is often assumed to be a hallmark of electron−electron scattering in Fermi liquid metals,[39] and the 6.2 GPa data for R = F is well fitted to this model (see Figure S14). However, in a 2D Fermi liquid, electron−electron scattering is predicted either to give rise to a
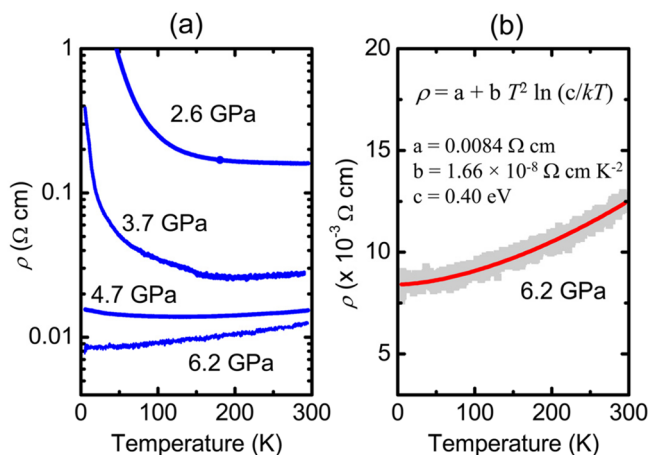
Figure 15. (a) Plots of resistivity ρ versus temperature for **2** (R = F) at selected pressures, measured using a DAC. (b) Expansion of resistivity (ρ) versus T plot at P = 6.2 GPa, with calculated fit (in red) to $\rho(T) = a + bT \ln[c/kT]$, where $c = \varepsilon_F - \varepsilon_B$.

slightly weaker power law dependence[40] or to contain logarithmic corrections.[41] Consistently a fit to the variable exponent function $\rho(T) = \rho_0 + AT^n$ affords a better fit with a value of $n = 1.65$, and the data can be equally well modeled by $\rho(T) = \rho_0 + AT^2 \ln[k(\varepsilon_F - \varepsilon_B)/T]$ with $(\varepsilon_F - \varepsilon_B) = 0.4$ eV (as shown in Figure 15b), consistent with the energy scale predicted by the DFT band structure calculations discussed in the following section (Band Structure Calculations). However, the extended range (to 300 K) of this temperature dependence is unusual, as other scattering processes are usually expected to dominate at higher temperatures. In this context, it is worth noting that scattering of metallic electrons from phonons[42] and magnetic excitations[43] may also provide a quasiquadratic temperature dependence of resistivity under specific circumstances.[44]

Band Structure Calculations. In an earlier section (Theoretical Model) of this paper we demonstrated that the total kinetic stabilization of the metallic state of a multiorbital radical ΔE_k could be expressed as the sum of two components (Figure 5), one ($\Delta\mu$) arising from a lowering of the Fermi level (ε_F) relative to the Mott state (ε_0) occasioned by electron redistribution between the SOMO and LUMO bands, and the other stemming from the dispersion effects, that is, the delocalization of electrons within these bands (ε_{dis}), which lowers the average kinetic energy per electron (ε_{ave}) relative to ε_F. To illustrate the applicability of these concepts to the present systems, we have carried out a series of DFT band structure calculations on **2** (R = H, F, Ph) in order to estimate the pressure dependence of both $\Delta\mu$ and ε_{dis}. The calculations were based on atomic coordinates taken from the high-pressure structural data and used the Quantum Espresso package with ultrasoft PBE pseudopotentials and a plane-wave cutoff of 25 Ry and a 250 Ry integration mesh. The results were analyzed using the WANNIER90 code[45] to generate a tight-binding model including the SOMO energy ε_0, which was obtained after rotation of the resulting Hamiltonian into diagonal form at each site.

The results are presented in Figure 16, in the form of plots of densities of states $D(\varepsilon)$ for **2** (R = H, F, Ph) at low and high pressures. From these calculations, and others at intermediate pressures, values for the various contributions ($\Delta\mu$ and ε_{dis}) to the total kinetic energy (ΔE_k) as a function of pressure were
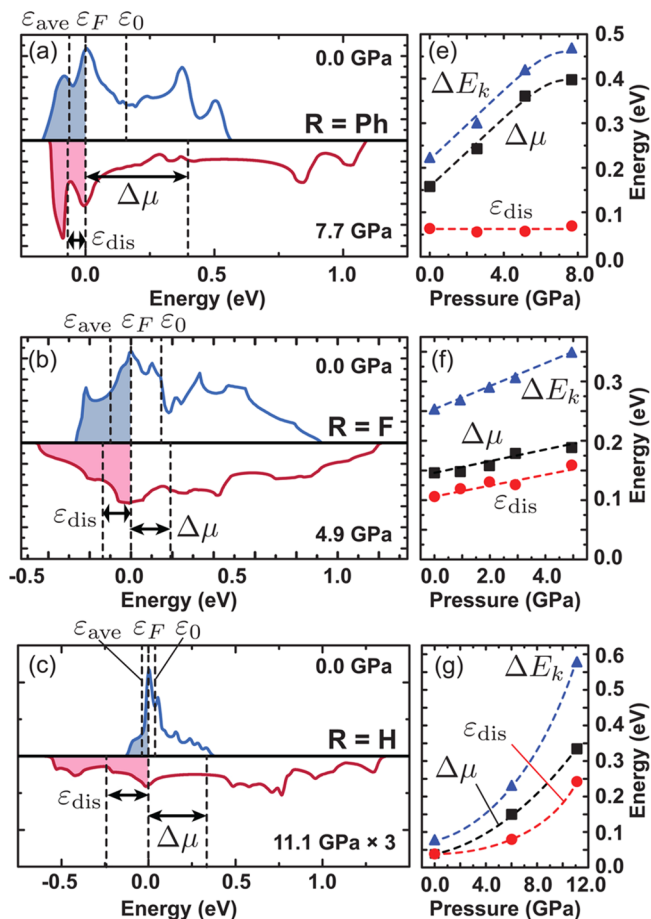
Figure 16. (a–c) Pairs of plots of the total density of states $D(\varepsilon)$ (vertical axis) for **2** (R = Ph, F, H), one calculated at 0 GPa and another at a pressure close to or above the onset of metallization. Occupied levels are shaded, and the Fermi level is indicated by ε_F, while the average and lowest occupied levels are ε_{ave} and ε_B, and the multiorbital redistribution energy $\Delta\mu = \varepsilon_0 - \varepsilon_F$ are indicated with dashed lines; the dispersion energy $\varepsilon_{dis} = \varepsilon_F - \varepsilon_{ave}$. (d–g) Plots of $\Delta\mu$, the dispersion energy ε_{dis}, and the total kinetic stabilization $\Delta E_k = \varepsilon_{dis} + \Delta\mu$ as a function of pressure.

extracted (see Table S2). By way of a caveat we note that these calculations implicitly assume a metallic state and, as such, show no charge gap at any pressure; they represent a zeroth-order approximation for the high-pressure metallic state. In all three materials, $\Delta\mu$ represents the dominant contribution to the kinetic stabilization, implying strong mixing of the SOMO and LUMO (a large $t_{ij}^{01}/\Delta\varepsilon$ ratio) or a large discrepancy in the natural width (a large t_{ij}^{11}/t_{ij}^{00} ratio), so that the two orbitals may strongly overlap. This result is not surprising given the prevalence for ferromagnetic interactions in the ambient pressure magnetic response of all three materials.[20,21]

For **2** (R = Ph), a relatively 1D electronic structure is predicted at all pressures, as evidenced by the bimodal shape of $D(\varepsilon)$, and very strong overlap of the SOMO and LUMO bands results in an essentially 1/4-filled state. A peculiarity of this case is that ε_{dis} is essentially pressure independent, while $\Delta\mu$ sharply increases with pressure. Despite a relatively large value predicted for ΔE_k, **2** (R = Ph) displays the largest activation energy at ambient pressure of all three materials, which only approaches zero near 10 GPa. In this context, it is worth noting that 1D systems with one particle per site should display an essentially insulating ground state for any finite interaction U,

V, and thus the response of **2** (R = Ph) may be ascribed to its low dimensionality.[46] For the higher dimensional materials **2** (R = F, H), we find a threshold value of the total kinetic stabilization $\Delta E_k = \varepsilon_{dis} + \Delta\mu \sim 0.25$–0.3 eV corresponding to the experimental pressure of metallization (at ∼3 and ∼6 GPa) in the respective materials. Given the optical measurement of $U_{eff} \sim 0.6$–0.8 eV, we may estimate that $U_C \sim 3\Delta E_k$, which is consistent with the suggested condition $U_C/\Delta E_k \lesssim 4$ but may indicate a magnetic origin for the insulating behavior at intermediate pressure. For **2** (R = F), the electronic dispersion is already well developed at ambient pressure, such that ΔE_k increases only moderately upon compression, with the calculated Fermi energy, which may be approximated by ($\varepsilon_F - \varepsilon_B$), reaching a value (at 4.9 GPa) near 0.5 eV, which is comparable to that extracted (∼0.4 eV) from the logarithmic $\rho(T)$ analysis of the DAC data at 6.2 GPa (Figure 15b).

Finally, and in contrast to the R = F compound, the ambient pressure structure of the R = H derivative displays exceedingly small dispersion of both the SOMO and LUMO, leading to small values of both $\Delta\mu$ and ε_{dis}. It is only after undergoing a structural phase transition from the α- to β-phase that ΔE_k is able to reach the threshold value for metallization. However, in both materials, the dominant contributor over the entire pressure range is the multiorbital electron redistribution term $\Delta\mu$. This result is profound, as it clearly demonstrates that the relative ease of metallization of **2** (R = F, H) can be attributed in large part to the additional degrees of freedom provided by the overlap and mixing of energy bands associated with the SOMO and LUMO.

SUMMARY AND CONCLUSIONS

From a practical perspective, efforts to build an organic radical-based conductor have always suffered from a serious energetic mismatch; the potential energy cost (U) of site-to-site transfer of an unpaired electron is much larger than the kinetic stabilization (W) afforded by charge delocalization into a half-filled energy band. Perhaps predictably, attempts to alter the U/W balance have focused on the use of spin delocalization to lower U[1b−d] and the incorporation of heavy p-block heteroatoms (S, Se) to enhance intermolecular overlap and increase W.[10] Alternatively, performance can be improved by relaxing the classical prescription for a perfectly half-filled band, that is, the one-electron, one-orbital paradigm. Thus, in mixed-valence spirobiphenalenyls[6,7] and in chemically doped radical ion salts,[47] the effective Coulomb barrier U_{eff} is reduced as additional channels for charge transport become available.

In the oxobenzene-bridged bisdithiazolyl radicals **2** considered here, a lowering in U_{eff} is achieved by means of an enhanced electron affinity afforded by low-lying open-shell anionic states made available by the low-lying LUMO (Figure 2). At the same time overlap and mixing of energy bands based on the LUMO and SOMO opens up new degrees of freedom for the kinetic stabilization (ΔE_k) of the metallic state. In addition to the contribution to ΔE_k arising from delocalization of electrons ($\varepsilon_{dis} = \varepsilon_F - \varepsilon_{ave}$) within these bands, the redistribution of electrons between the SOMO and LUMO bands lowers the Fermi level relative to the Mott state (Figure 5). Indeed, when R = F, H, this latter multiorbital term ($\Delta\mu = \varepsilon_0 - \varepsilon_F$) accounts for well over half of the total kinetic stabilization of the metallic state. If it were *not* present, that is, if $\Delta\mu = 0$, the delocalization term ε_{dis} for R = F (Figure 16) would have to increase to near 0.3 eV to make up the deficit and generate a value of ΔE_k sufficient to stabilize the metallic state.

Extrapolation of ε_{dis} to reach that value indicates that, under such conditions, metallization of **2** (R = F) would require pressurization to near 24 GPa. It is therefore not surprising that pressure-induced metallization of radicals **1** has not been achieved without the use of Se-incorporation (chemical pressure).[12]

In the three multiorbital radicals **2** (R = F, H, Ph) the combination of a reduced U_{eff} and a large $\Delta\mu$ is sufficient to afford a bad metal state near 3, 6, and 12 GPa, respectively. The wide range of pressure across the set required to produce this result serves to illustrate the importance of structural and hence electronic dimensionality on transport properties. Culminating this work is the observation of a quasiquadratic temperature dependence (from 5 to 300 K) of the resistivity found near 6 GPa for the 2D R = F material, which provides strong evidence for the formation of a Fermi liquid metallic state.[40,41] This is, we believe, the first such finding for a neutral radical conductor. Overall, the experimental and computational results augur well for the design of new metallic and perhaps superconducting materials based on the multiorbital radical concept. To this end, understanding and exploring the effect of variations in the basal R-group on the size of the SOMO−LUMO gap, and hence U_{eff} and ΔE_k, will play an important role in future work.

EXPERIMENTAL SECTION

Sample Preparation. High-purity polycrystalline samples of **2** (R = H, F, Ph) suitable for high-pressure crystallographic, conductivity, and optical measurements were prepared by reduction of the corresponding salts [**2**][OTf] (OTf = trifluoromethanesulfonate) with octamethylferrocene in degassed acetonitrile. Details are described elsewhere.[16a,d,e]

Powder Crystallography. High-pressure diffraction experiments on **2** (R = F, Ph), analogous to those performed earlier for R = H,[20] were carried out on beamline BL10XU at SPring-8, using synchrotron radiation (λ= 0.41244 Å) and powdered samples mounted in a DAC, with helium as the pressure transmitting medium. (At room temperature, helium stays in a liquid state up to 14 GPa, hence providing hydrostatic pressure conditions.) For both compounds series of data sets were collected over the range $2\theta = 3$−30° at room temperature and as a function of increasing pressure from 0 to 10.0 GPa. Space group determinations, indexing, and refinement of cell parameters were performed using DASH 3.1.[48] The structures were solved starting from molecular models derived from the ambient pressure crystal structures. During the initial refinement in DASH, a rigid-body constraint was maintained. Final Rietveld[49] refinement, using fixed atomic positions and isotropic thermal parameters with an assigned value of 0.025, was performed in GSAS.[50] Atomic positions obtained from DASH were not further refined in GSAS, as a result of which standard deviations for atomic coordinates are not reported in the CIF files.

Magnetic Measurements. DC magnetic susceptibility measurements on samples of **2** (R = Ph, H) were performed using a PCC[51] over the pressure range 0−1.0 GPa (R = Ph) and 0−1.5 GPa (R = H) in a SQUID magnetometer. The crystals were mixed with a pressure transmitting medium, Fluorinert FC70 oil. Pressure estimation was performed by calibration of pressure versus load.

Multi-Anvil Press (MAP) Conductivity Measurements. High-pressure conductivity experiments on **2** (R = H, F, Ph) were performed in a 3000-ton MAP using a Cr_2O_3-doped MgO octahedron as the pressure transmitting medium.[52] The pressure was generated by three electric oil pumps, transmitted through a split-cylinder module to six steel anvils, then to eight tungsten carbide (WC) cubes with 32 mm edge length, and finally through the eight truncated corners of these cubes to the octahedral pressure medium. The force−pressure relationships for the 18/11 and 14/8 (octahedral-edge-length (mm)/truncated-edge-length (mm)) cell configurations adopted in these experiments were determined from prior calibrations of the

applied hydraulic load against pressures of structure transformations in standards at room temperature (Bi I ↔ II at 2.55 GPa, Bi III ↔ V at 7.7 GPa, Sn I ↔ II at 9.4 GPa, and Pb I ↔ II at 13.4 GPa). The pressure cell was modified to include a cylindrical heater made from a rhenium (Re) foil of 0.05 mm thickness and a $W_5Re_{95}/W_{26}Re_{74}$ thermocouple with its junction placed in contact with the outside wall of the Re heater. Powder samples were densely packed in a boron nitride ($\sigma_{BN} = 10^{-11}$ S cm^{-1}) cup with Pt disk electrodes in direct contact with the samples at both ends. Four wire AC (Solartron 1260 Impedance Analyzer) resistance measurements were made at a frequency of 1 kHz. A series of resistance measurements was performed at pressures up to 10−15 GPa and temperatures ranging from 298 to 370 K. In each series, the pressure was first increased to the target value, and then resistance measurements were made at fixed temperature intervals of 10 K on heating/cooling at constant pressure. The contiguous cylinder-shaped sample was extracted from the recovered pressure cell, and the sample geometry was measured to convert resistance to conductivity. For convenience, the term σ_{RT} refers to the conductivity measured at 298 K. Improvements made in the assessment of lead resistance have been applied to all large volume press resistivity data shown here. As a result the values of σ_{RT} and E_{act} provided in Figure 11 differ slightly from those reported earlier,[16d,20] but the pressure-dependent behavior remains unchanged.

Diamond Anvil Cell (DAC) Resistance Measurements. High-pressure electrical resistance measurements on **2** (R = H) were performed using the four-probe technique in a DAC. Pressure was generated by a pair of diamonds with a 600 μm diameter culet. A sample hole of 300 μm diameter was drilled in the gasket after its thickness was reduced from 250 to 30 μm by preindentation. It was then covered with a thin layer of cubic boron nitride (BN) for electrical insulation between the gasket and the electrodes. Gold wire of 18 μm diameter was used as electrode leads. The pressure was determined by the ruby fluorescence method at room temperature before and after each cooling cycle. A similar arrangement was used for high-pressure transport measurements on **2** (R = F). A 250 μm stainless steel gasket was first indented to around 50 μm thick, with two opposing 600 μm diamond anvils in a piston cylinder pressure cell setting. A 300 μm sample area was then drilled out and insulated with a thin alumina layer. Before the sample area was tightly packed with ruby chips and powdered sample, four gold contacts were attached along the rim of the hole. For both R = H and F the resistance was converted to resistivity by calibration against the MAP measurements.

Optical Measurements. The optical conductivity measurements on **2** (R = H, F) were obtained under pressure based on reflectivity measurements conducted at the U2A beamline sidestation of the NSLS3. Infrared spectra were collected using a Bruker Vertex 80v FTIR spectrometer and a Hyperion 2000 IR microscope attached with an MCT detector on pressed powder samples in a DAC with KBr as a pressure transfer medium. Optical conductivity σ_1 as a function of pressure (Figure 12) was obtained by Kramers−Kronig (K-K) analysis of normal incidence reflectivity measurements. For this purpose, strong phonon bands in the region from 1700 to 2700 cm^{-1} originating from the diamond cell were omitted by replacing this spectral region by a straight line interpolation. The resulting reflectivity data, after correction for the diamond refractive index, were then fit using a variational K-K constrained dielectric function, as implemented in the REFFIT code.[34]

Electronic Structure Calculations. Band structure calculations were carried out with the QUANTUM ESPRESSO[53] package using Perdew−Burke−Ernzerhof functionals[54] and ultrasoft pseudopotentials with a plane-wave cutoff of 25 Ry and a 250 Ry integration mesh. Geometrical coordinates were taken from the single crystal structures and GSAS refined high -pressure powder data. In the case of **2** (R = H) the calculations were performed on the primitive cell. The SCF calculations employed a 4 × 4 × 4 Monkhorst−Pack k-point mesh. The resulting energy parameters $\Delta\mu$, ε_{dis}, and ΔE_k plotted in Figure 16 and listed in Table S2.

ASSOCIATED CONTENT

Ⓢ Supporting Information

The Supporting Information is available free of charge on the ACS Publications website at DOI: 10.1021/jacs.5b08254.

> PXRD for **2** (R = F) at 1.0 GPa (CIF)
> PXRD for **2** (R = F) at 2.0 GPa (CIF)
> PXRD for **2** (R = F) at 2.9 GPa (CIF)
> PXRD for **2** (R = F) at 4.3 GPa (CIF)
> PXRD for **2** (R = F) at 5.0 GPa (CIF)
> PXRD for **2** (R = F) at 6.1 GPa (CIF)
> PXRD for **2** (R = F) at 8.9 GPa (CIF)
> PXRD for **2** (R = Ph) at 2.6 GPa (CIF)
> PXRD for **2** (R = Ph) at 5.5 GPa (CIF)
> PXRD for **2** (R = Ph) at 7.7 GPa (CIF)
> PXRD for **2** (R = Ph) at 10.1 GPa (CIF)
> Details of crystallographic data collection and structure refinement, resistivity data fits, and of the electronic band structure calculations (PDF)

AUTHOR INFORMATION

Corresponding Author

*oakley@uwaterloo.ca

Notes

The authors declare no competing financial interest.

REFERENCES

(1) (a) McCoy, N. H.; Moore, W. C. *J. Am. Chem. Soc.* **1911**, *33*, 273. (b) Haddon, R. C. *Nature* **1975**, *256*, 394. (c) Haddon, R. C. *Aust. J. Chem.* **1975**, *28*, 2333. (d) Haddon, R. C. *Aust. J. Chem.* **1975**, *28*, 2343.

(2) (a) Rawson, J. M.; Alberola, A.; Whalley, A. *J. Mater. Chem.* **2006**, *16*, 2560. (b) Hicks, R. G. In *Stable Radicals: Fundamentals and Applied Aspects of Odd-Electron Compounds*; Hicks, R. G., Ed.; John Wiley & Sons, Ltd.: Wiltshire, 2010; pp 317−380. (c) Boeré, R. T.; Roemmele, T. L. *Comp. Inorg. Chem. II* **2013**, *1*, 375. (d) Haddon, R. C. *ChemPhysChem* **2012**, *13*, 3581. Saito, G.; Yoshida, Y. *Bull. Chem. Soc. Jpn.* **2007**, *80*, 1. (e) Saito, G.; Yoshida, Y. *Top. Curr. Chem.* **2012**, *312*, 67. Ratera, I.; Veciana, J. *Chem. Soc. Rev.* **2012**, *41*, 303.

(3) Mou, Z.; Uchida, K.; Kubo, T.; Kertesz, M. *J. Am. Chem. Soc.* **2014**, *136*, 18009. (b) Small, D.; Zeitsev, V.; Jung, Y. S.; Rosokha, S. V.; Head-Gordon, M.; Kochi, J. K. *J. Am. Chem. Soc.* **2004**, *126*, 13850. (c) Huang, J.; Kertesz, M. *J. Am. Chem. Soc.* **2007**, *129*, 1634. (d) Takano, Y.; Taniguchi, T.; Isobe, H.; Kubo, T.; Morita, Y.; Yamamoto, K.; Nakasuji, K.; Takui, T.; Yamaguchi, K. *J. Am. Chem. Soc.* **2002**, *124*, 11122. (e) Beer, L.; Mandal, S. K.; Reed, R. W.; Oakley, R. T.; Tham, F. S.; Donnadieu, B.; Haddon, R. C. *Cryst. Growth Des.* **2007**, *7*, 802.

(4) (a) Oakley, R. T. *Prog. Inorg. Chem.* **1988**, *36*, 299. (b) Rawson, J. M.; Banister, A. J.; Lavender, I. *Adv. Heterocycl. Chem.* **1995**, *62*, 137. (c) Haynes, D. A. *CrystEngComm* **2011**, *13*, 4793. (d) Beneberu, H. Z.; Tian, Y.-H.; Kertesz, M. *Phys. Chem. Chem. Phys.* **2012**, *14*, 10713. (e) Preuss, K. E. *Polyhedron* **2014**, *79*, 1. (f) Cui, Z.; Lischka, H.;

Beneberu, H. Z.; Kertesz, M. *J. Am. Chem. Soc.* **2014**, *136*, 12958.
(g) Tian, Y.-H.; Sumpter, B. G.; Du, S.; Huang, J. *J. Phys. Chem. Lett.* **2015**, *6*, 2318. (h) Yutronkie, N. J.; Leitch, A. A.; Korobkov, I.; Brusso, J. L. *Cryst. Growth Des.* **2015**, *15*, 2524.

(5) (a) Mott, N. F. *Proc. Phys. Soc., London, Sect. A* **1949**, *62*, 416.
(b) Mott, N. F. *Metal-insulator Transitions*; Taylor and Francis: London, 1990.

(6) (a) Chi, X.; Itkis, M. E.; Patrick, B. O.; Barclay, T. M.; Reed, R. W.; Oakley, R. T.; Cordes, A. W.; Haddon, R. C. *J. Am. Chem. Soc.* **1999**, *121*, 10395. (b) Goto, K.; Kubo, T.; Yamamoto, K.; Nakasuji, K.; Sato, K.; Shiomi, D.; Takui, T.; Kubota, M.; Kobayashi, T.; Yakusi, K.; Ouyang, J. *J. Am. Chem. Soc.* **1999**, *121*, 1619. (c) Mandal, S. K.; Samanta, S.; Itkis, M. E.; Jensen, D. W.; Reed, R. W.; Oakley, R. T.; Tham, F. S.; Donnadieu, B.; Haddon, R. C. *J. Am. Chem. Soc.* **2006**, *128*, 1982. (d) Pal, S. K.; Itkis, M. E.; Tham, F. S.; Reed, R. W.; Oakley, R. T.; Haddon, R. C. *J. Am. Chem. Soc.* **2008**, *130*, 3942. (e) Morita, Y.; Suzuki, S.; Sato, K.; Takui, T. *Nat. Chem.* **2011**, *3*, 197. (f) Nishida, S.; Kawai, J.; Moriguchi, M.; Ohba, T.; Haneda, N.; Fukui, K.; Fuyuhiro, A.; Shiomi, D.; Sato, K.; Takui, T.; Nakasuji, K.; Morita, Y. *Chem. - Eur. J.* **2013**, *19*, 11904.

(7) (a) Haddon, R. C.; Sarkar, A.; Pal, S. K.; Chi, X.; Itkis, M. E.; Tham, F. S. *J. Am. Chem. Soc.* **2008**, *130*, 13683. (b) Bag, P.; Itkis, M. E.; Pal, S. K.; Donnadieu, B.; Tham, F. S.; Park, H.; Schlueter, J. A.; Siegrist, T.; Haddon, R. C. *J. Am. Chem. Soc.* **2010**, *132*, 2684. (c) Huang, J.; Kertesz, M. J. *J. Am. Chem. Soc.* **2003**, *125*, 13334. (d) Huang, J.; Kertesz, M. J. *Am. Chem. Soc.* **2007**, *129*, 1634. (e) Bohlin, J.; Hansson, A.; Stafstrom, S. *Phys. Rev. B: Condens. Matter Mater. Phys.* **2006**, *74*, 155111. (f) Kubo, T.; Katada, Y.; Shimizu, A.; Hirao, Y.; Sato, K.; Takui, T.; Uruichi, M.; Yakushi, K.; Haddon, R. C. *J. Am. Chem. Soc.* **2011**, *133*, 14240. (g) Bag, P.; Pal, S. K.; Itkis, M. E.; Sarkar, S.; Tham, F. S.; Donnadieu, B.; Haddon, R. C. *J. Am. Chem. Soc.* **2013**, *135*, 12936.

(8) Pal, S. K.; Itkis, M. E.; Tham, F. S.; Reed, R. W.; Oakley, R. T.; Haddon, R. C. *Science* **2005**, *309*, 281.

(9) (a) Cordes, A. W.; Haddon, R. C.; Oakley, R. T. In *The Chemistry of Inorganic Ring Systems*, Steudel, R., Ed.; Elsevier: Amsterdam, 1992; pp 295−321. (b) Oakley, R. T. *Can. J. Chem.* **1993**, *71*, 1775.

(10) (a) Beer, L.; Brusso, J. L.; Cordes, A. W.; Haddon, R. C.; Itkis, M. E.; Kirschbaum, K.; MacGregor, D. S.; Oakley, R. T.; Pinkerton, A. A.; Reed, R. W. *J. Am. Chem. Soc.* **2002**, *124*, 9498. (b) Cordes, A. W.; Haddon, R. C.; Oakley, R. T. *Phosphorus, Sulfur Silicon Relat. Elem.* **2004**, *179*, 673. (c) Leitch, A. A.; Reed, R. W.; Robertson, C. M.; Britten, J. F.; Yu, X.; Secco, R. A.; Oakley, R. T. *J. Am. Chem. Soc.* **2007**, *129*, 7903.

(11) (a) Brusso, J. L.; Derakhshan, S.; Itkis, M. E.; Kleinke, H.; Haddon, R. C.; Oakley, R. T.; Reed, R. W.; Richardson, J. F.; Robertson, C. M.; Thompson, L. K. *Inorg. Chem.* **2006**, *45*, 10958. (b) Brusso, J. L.; Cvrkalj, K.; Leitch, A. A.; Oakley, R. T.; Reed, R. W.; Robertson, C. M. *J. Am. Chem. Soc.* **2006**, *128*, 15080. (c) Leitch, A. A.; Yu, X.; Winter, S. M.; Secco, R. A.; Dube, P. A.; Oakley, R. T. *J. Am. Chem. Soc.* **2009**, *131*, 7112.

(12) Leitch, A. A.; Lekin, K.; Winter, S. M.; Downie, L. E.; Tsuruda, H.; Tse, J. S.; Mito, M.; Desgreniers, S.; Dube, P. A.; Zhang, S.; Liu, Q.; Jin, C.; Ohishi, Y.; Oakley, R. T. *J. Am. Chem. Soc.* **2011**, *133*, 6051.

(13) (a) Robertson, C. M.; Leitch, A. A.; Cvrkalj, K.; Reed, R. W.; Myles, D. J. T.; Dube, P. A.; Oakley, R. T. *J. Am. Chem. Soc.* **2008**, *130*, 8414. (b) Robertson, C. M.; Leitch, A. A.; Cvrkalj, K.; Myles, D. J. T.; Reed, R. W.; Dube, P. A.; Oakley, R. T. *J. Am. Chem. Soc.* **2008**, *130*, 14791.

(14) Leitch, A. A.; Brusso, J. L.; Cvrkalj, K.; Reed, R. W.; Robertson, C. M.; Dube, P. A.; Oakley, R. T. *Chem. Commun.* **2007**, 3368.

(15) Desiraju, G. R. *Angew. Chem., Int. Ed. Engl.* **1995**, *34*, 2311.

(16) (a) Yu, X.; Mailman, A.; Dube, P. A.; Assoud, A.; Oakley, R. T. *Chem. Commun.* **2011**, *47*, 4655. (b) Yu, X.; Mailman, A.; Lekin, K.; Assoud, A.; Dube, P. A.; Oakley, R. T. *Cryst. Growth Des.* **2012**, *12*, 2485. (c) Yu, X.; Mailman, A.; Lekin, K.; Assoud, A.; Robertson, C. M.; Noll, B. C.; Campana, C. F.; Howard, J. A. K.; Dube, P. A.; Oakley, R. T. *J. Am. Chem. Soc.* **2012**, *134*, 2264. (d) Mailman, A.; Winter, S. M.; Yu, X.; Robertson, C. M.; Yong, W.; Tse, J. S.; Secco, R. A.; Liu,

Z.; Dube, P. A.; Howard, J. A. K.; Oakley, R. T. *J. Am. Chem. Soc.* **2012**, *134*, 9886. (e) Wong, J. W. L.; Mailman, A.; Winter, S. M.; Robertson, C. M.; Holmberg, R. J.; Murugesu, M.; Dube, P. A.; Oakley, R. T. *Chem. Commun.* **2014**, *50*, 785.

(17) Mailman, A.; Winter, S. M.; Wong, J. W. L.; Robertson, C. M.; Assoud, A.; Dube, P. A.; Oakley, R. T. *J. Am. Chem. Soc.* **2015**, *137*, 1044.

(18) The value of U may be approximated (in solution or in the gas phase) in terms of the disproportionation enthalpy ΔH_{disp} of two radicals into a cation/anion pair, i.e., $2R \rightleftarrows R^+ + R^-$, which is equal to the difference between the ionization potential (IP) and electron affinity (EA). The electrochemical cell potential E_{cell} is defined here as the numerical difference between the half-wave potentials for the oxidation and reduction steps, that is, $|E_{cell} = E_{1/2}(ox) - E_{1/2}(red)|$.

(19) Hoffmann, R. *Angew. Chem., Int. Ed. Engl.* **1982**, *21*, 711.

(20) Wong, J. W. L.; Mailman, A.; Lekin, K.; Winter, S. M.; Yong, W.; Zhao, J.; Garimella, S. V.; Tse, J. S.; Secco, R. A.; Desgreniers, S.; Ohishi, Y.; Borondics, F.; Oakley, R. T. *J. Am. Chem. Soc.* **2014**, *136*, 1070.

(21) Winter, S. M.; Mailman, A.; Oakley, R. T.; Thirunavukkuarasu, K.; Hill, S.; Graf, D. E.; Tozer, S. W.; Tse, J. S.; Mito, M.; Yamaguchi, H. *Phys. Rev. B: Condens. Matter Mater. Phys.* **2014**, *89*, 214403.

(22) (a) McWhan, D. B.; Remeika, J. P. *Phys. Rev. B* **1970**, *2*, 3734. (b) Limelette, P.; Georges, A.; Jerome, D.; Wzietek, P.; Metcalf, P.; Honig, J. M. *Science* **2003**, *302*, 89. (c) Yoon, C. O.; Reghu, M.; Moses, D.; Heeger, A. J. *Phys. Rev. B: Condens. Matter Mater. Phys.* **1994**, *49*, 10851.

(23) In radicals possessing a doubly occupied orbital close in energy to the SOMO, a triplet state cation can compete with the closed-shell singlet cation. See, for example: Nicolaides, A.; Smith, D. M.; Jensen, F.; Radom, L. *J. Am. Chem. Soc.* **1997**, *119*, 8083.

(24) Huang, J.; Kertesz, M. *J. Phys. Chem. A* **2007**, *111*, 6304.

(25) Hubbard, J. *Proc. R. Soc. London, Ser. A* **1963**, *276*, 238.

(26) Whangbo, M. H. *J. Chem. Phys.* **1979**, *70*, 4763.

(27) Balzer, M.; Kyung, B.; Sénéchal, D.; Tremblay, A.-M. S.; Potthoff, M. *Eur. Phys. Lett.* **2009**, *85*, 17002.

(28) Georges, A.; Kotliar, G.; Krauth, W.; Rozenberg, M. J. *Rev. Mod. Phys.* **1996**, *68*, 13.

(29) Leitch, A. A.; Reed, R. W.; Robertson, C. M.; Britten, J. F.; Yu, X.; Secco, R. A.; Oakley, R. T. *J. Am. Chem. Soc.* **2007**, *129*, 7903.

(30) (a) Anderson, P. W. *Phys. Rev.* **1959**, *115*, 2. (b) Goodenough, J. B. *J. Phys. Chem. Solids* **1958**, *6*, 287. Goodenough, J. B. *Magnetism and the Chemical Bond*; Interscience-Wiley: New York, 1963.

(31) (a) Catilla, G.; Chakravarty, S.; Emery, V. J. *Phys. Rev. Lett.* **1995**, *75*, 1823. (b) Hase, M.; Kuroe, H.; Ozawa, K.; Suzuki, O.; Kitazawa, H.; Kido, G.; Sekine, T. *Phys. Rev. B: Condens. Matter Mater. Phys.* **2004**, *70*, 104426. (c) Kumar, M.; Dutton, S. E.; Cava, R. J.; Soos, S. G. *J. Phys.: Condens. Matter* **2013**, *25*, 136004.

(32) Ioffe, A. F.; Regel, A. R. *Prog. Semicond.* **1960**, *4*, 237.

(33) (a) Basov, D. N.; Averitt, R. D.; van der Marel, D.; Dressel, M.; Haule, K. *Rev. Mod. Phys.* **2011**, *83*, 471. (b) Dressel, M.; Grüner, G. *Electrodynamics of Solids*; Cambridge University Press: Cambridge, 2002.

(34) Kuzmenko, A. B. *Rev. Sci. Instrum.* **2005**, *76*, 083108.

(35) (a) Götze, W.; Wölfle, P. *Phys. Rev. B* **1972**, *6*, 1226. (b) Allen, J. W.; Mikkelsen, J. C. *Phys. Rev. B* **1977**, *15*, 2952.

(36) (a) Chui, T.; Deutscher, G.; Lindenfeld, P.; McLean, W. L. *Phys. Rev. B: Condens. Matter Mater. Phys.* **1981**, *23*, 6172. (b) Mott, N. F.; Kaveh, M. *Adv. Phys.* **1985**, *34*, 329. (c) Rapp, Ö.; Bhagat, S. M.; Gudmundsson, H. *Solid State Commun.* **1982**, *42*, 741. (d) Lee, P. A.; Ramakrishnan, T. V. *Rev. Mod. Phys.* **1985**, *57*, 287. (e) Meikap, A. K.; Chen, Y. Y.; Lin, J. J. *Phys. Rev. B: Condens. Matter Mater. Phys.* **2004**, *69*, 212202.

(37) (a) Kurosaki, Y.; Shimizu, Y.; Miyagawa, K.; Kanoda, K.; Saito, G. *Phys. Rev. Lett.* **2005**, *95*, 177001. (b) Dressel, M.; Degiorgi, L.; Klein, O.; Gruner, G. *J. Phys. Chem. Solids* **1993**, *54*, 1411. (c) Bulaevskii, L. N. *Adv. Phys.* **1988**, *37*, 443.

(38) Barišić, N.; Chan, M. K.; Li, Y.; Yu, G.; Zhao, X.; Dressel, M.; Smontara, A.; Greven, M. *Proc. Natl. Acad. Sci. U. S. A.* **2013**, *110*, 12235.

(39) (a) Landau, L. D.; Pomeranchuk, I. J. *Phys. Z. Sowjetunion* **1936**, *10*, 649. (b) Landau, L. D.; Pomeranchuk, I. J. *Zh. Eksp. Teor. Fiz.* **1937**, *7*, 379. (c) Baber, W. G. *Proc. R. Soc. London, Ser. A* **1937**, *158*, 383.

(40) Kaveh, M.; Wiser, N. *Adv. Phys.* **1984**, *33*, 257.

(41) (a) Giuliani, G. F.; Quinn, J. J. *Phys. Rev. B: Condens. Matter Mater. Phys.* **1982**, *26*, 4421. (b) Chaplik, A. V. *Soviet Phys. JETP* **1971**, *33*, 99. (c) Hodges, C.; Smith, H.; Wilkins, J. W. *Phys. Rev. B* **1971**, *4*, 302.

(42) (a) Crespi, V. H.; Hou, J. G.; Xiang, X.-D.; Cohen, M. L.; Zettl, A. *Phys. Rev. B: Condens. Matter Mater. Phys.* **1992**, *46*, 12064. (b) Kaveh, M.; Cherry, M. F. *J. Phys. C: Solid State Phys.* **1981**, *14*, L789.

(43) Volkenshtein, N. V.; Dyakina, V. P.; Startsev, V. E. *Phys. Status Solidi B* **1973**, *57*, 9.

(44) (a) Kiss, T.; Chainani, A.; Yamamoto, H. M.; Miyazaki, T.; Akimoto, T.; Shimojima, T.; Ishizaka, K.; Watanabe, S.; Chen, C.-T; Fukaya, A.; Kato, R.; Shin, S. *Nat. Commun.* **2012**, *3*, 1089. (b) Roshkov, A. V. *Phys. Rev. Lett.* **2014**, *112*, 106403.

(45) (a) Mostofi, A. A.; Yates, J. R.; Lee, Y.-S.; Souza, I.; Vanderbilt, D.; Marzari, N. *Comput. Phys. Commun.* **2008**, *178*, 685. (b) Souza, I.; Marzari, N.; Vanderbilt, N. *Phys. Rev. B: Condens. Matter Mater. Phys.* **2001**, *65*, 035109.

(46) (a) Tomonaga, S. *Prog. Theor. Phys.* **1950**, *5*, 544. (b) Luttinger, J. M. *J. Math. Phys.* **1963**, *4*, 1154. (c) Giarmarchi, T. *Chem. Rev.* **2004**, *104*, 5037. (d) Giamarchi, T. *Quantum Physics in One Dimension*; Oxford University Press: Oxford, 2004.

(47) (a) Bryan, C. D.; Cordes, A. W.; Haddon, R. C.; Glarum, S. H.; Hicks, R. G.; Kennepohl, D. K.; MacKinnon, C. D.; Oakley, R. T.; Palstra, T. T. M.; Perel, A. S.; Schneemeyer, L. F.; Scott, S. R.; Waszczak, J. V. *J. Am. Chem. Soc.* **1994**, *116*, 1205. (b) Bryan, C. D.; Cordes, A. W.; Fleming, R. M.; George, N. A.; Glarum, S. H.; Haddon, R. C.; MacKinnon, C. D.; Oakley, R. T.; Palstra, T. T. M.; Perel, A. S. *J. Am. Chem. Soc.* **1995**, *117*, 6880. (c) Bryan, C. D.; Cordes, A. W.; Goddard, J. D.; Haddon, R. C.; Hicks, R. G.; MacKinnon, C. D.; Mawhinney, R. C.; Oakley, R. T.; Palstra, T. T. M.; Perel, A. S. *J. Am. Chem. Soc.* **1996**, *118*, 330.

(48) David, W. I. F.; Shankland, K.; van de Streek, J.; Pidcock, E.; Motherwell, W. D. S.; Cole, J. C. *J. Appl. Crystallogr.* **2006**, *39*, 910.

(49) Rietveld, H. M. *J. Appl. Crystallogr.* **1969**, *2*, 65.

(50) Larson, A. C.; Von Dreele, R. B. *General Structure Analysis System (GSAS)*; Technical Report for Los Alamos National Laboratory, Report LAUR 86-748: Los Alamos, NM, 2000.

(51) Mito, M. *J. Phys. Soc. Jpn.* **2007**, *76*, 182.

(52) Secco, R. A.; Yong, W.; Officer, T. *New 3000 Ton Multi-Anvil Press at the University of Western Ontario*, Abstract MR51A-02. Proceedings of the American Geophysical Union Meeting, Cancun, Mexico, May 14−17, 2013; AGU: Washington, D.C., 2013.

(53) Giannozzi, P.; Baroni, S.; Bonini, N.; Calandra, M.; Car, R.; Cavazzoni, C.; Ceresoli, D.; Chiarotti, G. L.; Cococcioni, M.; Dabo, I.; Dal Corso, A.; Fabris, S.; Fratesi, G.; de Gironcoli, S.; Gebauer, R.; Gerstmann, U.; Gougoussis, C.; Kokalj, A.; Lazzeri, M.; Martin-Samos, L.; Marzari, N.; Mauri, F.; Mazzarello, R.; Paolini, S.; Pasquarello, A.; Paulatto, L.; Sbraccia, C.; Scandolo, S.; Sclauzero, G.; Seitsonen, A. P.; Smogunov, A.; Umari, P.; Wentzcovitch, R. M. *J. Phys.: Condens. Matter* **2009**, *21*, 395502.

(54) (a) Perdew, J. P.; Burke, K.; Ernzerhof, M. *Phys. Rev. Lett.* **1996**, *77*, 3865. (b) Perdew, J. P.; Burke, K.; Ernzerhof, M. *Phys. Rev. Lett.* **1997**, *78*, 1396.